

Upper crustal structure beneath the Qin-Hang and Wuyishan metallogenic belts in Southeast China as revealed by a joint active and passive seismic experiment

Mengjie Zheng^{1b},^{1,2} Tao Xu^{1b},^{1,3} Qingtian Lü,⁴ Jiyan Lin,^{1,2,5} Minfu Huang,^{1,2} Zhiming Bai,¹ Yangfan Deng,⁶ Yongqian Zhang⁴ and José Badal⁷

¹State Key Laboratory of Lithospheric Evolution, Institute of Geology and Geophysics, Chinese Academy of Sciences, Beijing 100029, China.
E-mail: xutao@mail.iggcas.ac.cn

²University of Chinese Academy of Sciences, Beijing 100049, China

³Innovation Academy for Earth Science, Chinese Academy of Sciences, Beijing 100029, China

⁴Chinese Academy of Geological Sciences, Beijing 100037, China, lqt@cags.ac.cn. E-mail:

⁵Geophysical Exploration Center, China Earthquake Administration, Zhengzhou 450002, China

⁶State Key Laboratory of Isotope Geochemistry, Guangzhou Institute of Geochemistry, Chinese Academy of Sciences, Guangzhou 510640, China

⁷Physics of the Earth, Sciences B, University of Zaragoza, Pedro Cerbuna 12, Zaragoza 50009, Spain

Accepted 2022 August 18. Received 2022 August 17; in original form 2021 November 19

SUMMARY

Southeast China is one of the most important polymetallic metallogenic provinces in the world. However, distinct differences in the type and origin of the mineral deposits are present between the major metallogenic belts in this province. To deepen our knowledge of this regional metallogenic setting, investigate the factors controlling its metallogenic differences and explore the feasibility of active and passive seismic imaging, we performed a multibatch seismic experiment using active and passive sources with the help of 437 short-period seismographs deployed across the Qin-Hang and Wuyishan metallogenic belts in Southeast China. We resolved the *S*-wave velocity structure beneath the profile using ambient noise tomography and derived a *V_p/V_s* model by combining with a published *P*-wave model. A good correlation between the obtained seismic velocity models and geological observations is observed. The Proterozoic volcanic-sedimentary rock series and the Fuzhou-Yongfeng sedimentary basin are identified by low *P*- and *S*-wave velocities, high *V_p/V_s* ratios and low *S*-wave velocity perturbations. Within the core of the Wuyishan Metallogenic Belt, several narrow, elongated and low seismic velocity anomalies are considered to be signs of the nearby fault zones, and these anomalies provide reference information on the extension and pattern of these faults at depth. Combined with the geological and mineralogical evidence, we propose that these faults function as ore-guiding structures and facilitate the formation of regionally representative mineral species and metal assemblages.

Key words: Crustal imaging; Seismic interferometry; Crustal structure.

1 INTRODUCTION

Southeast China, tectonically referring to the Cathaysian Block and the Jiangnan orogenic belt on the northwestern margin of the block, is one of the most important metallogenic provinces of nonferrous, rare, rare earth and precious metals and is globally famous for its massive multiple-stage granites accompanied by large-scale and unique Mesozoic metallogeny of W, Sn, Cu, Fe, Pb, Zn, U, Nb and Ta (Mao *et al.* 2009; Li *et al.* 2013; Xing *et al.* 2017). Numerous studies have been conducted on the area's granites and related mineral deposits, and a general consensus has been reached on several issues, such as the timing, genetic types, spatial variation regularities, and

tectonic setting of granitic magmatism and metallogeny in South China (Sun 2006; Mao *et al.* 2009; He & Santosh 2016; Xing *et al.* 2017 and references therein). However, studies have also shown that the compositions of the granitoid intrusions and the types of mineral deposits in the Qin-Hang and Wuyishan metallogenic belts, the two most important metallogenic belts in the South China region, are distinctly different. For example, mineral deposits in the former belt are dominated by Cu–Pb–Zn polymetallic deposits of the porphyry-skarn types, which are likely mainly related to Early Jurassic *S*-type granites with meta- to weakly peraluminous features, whereas those in the latter belt are mainly Sn–Wn–Nb–Ta–U deposits chiefly related to highly fractionated I- and A-type granites

of a strongly para-aluminum series. The reasons and mechanisms that control these differences remain unexplored.

The formation of ore deposits is widely regarded as a shallow response to deep processes in the Earth's interior. Thus, the exploration and knowledge of the crustal and lithospheric architecture beneath key metallogenic zones are important for comprehensively understanding the regional tectonic evolution and formation of mineral deposits and can even guide the prospecting and mining of mineral resources. For example, O'Donnell *et al.* (2020) demonstrated the feasibility of using seismic tomography in mineral exploration and summarized the available and potential techniques and approaches. In South China, several geophysical studies have been conducted, including a *P*-wave tomography model revealing a remarkable correlation between the deposits and deep-seated, low-velocity, *P*-wave anomalies (He & Santosh 2016), a receiver function analysis showing that the Wuyishan Metallogenic Belt and the northern segment of the Qin-Hang Metallogenic Belt are characterized by a high V_p/V_s ratio (Zhang *et al.* 2021a), and a dense seismic array indicating a low velocity in the upper crust and a high velocity and a relatively high V_p/V_s ratio in the middle-lower crust beneath the Dahutang deposit (South China) (Zhang *et al.* 2021b). Although previous geophysical studies are helpful for understanding the regional metallogenic setting, few studies have focused on the shallow fine structure of the crust, which is particularly important for understanding the structures associated with the metallogeny because mineral deposits generally form in the shallow crust. In addition, the causes and controlling factors of regional metallogenic differences are still poorly understood because there are relatively few comprehensive studies across different metallogenic belts.

To better understand the structural features below the main metallogenic belts in Southeast China and explore the feasibility of active and passive seismic imaging, we deployed a seismic array between Wanzai and Yongchun across the Qin-Hang and Wuyishan metallogenic belts and conducted a joint active- and passive-source seismic experiment (Fig. 1). This paper presents the upper crustal seismic wave models obtained from the Wanzai-Yongchun profile including an *S*-wave velocity model revealed by ambient noise tomography and a derived V_p/V_s model combined with the previous *P*-wave model (Lin *et al.* 2020, 2021) and discusses their implications for metallogenic settings in Southeast China.

2 GEOLOGICAL SETTINGS

The South China Block, located at the southeastern edge of the Eurasian continent and the western end of the Pacific Ocean, was formed by the collision and amalgamation of the Cathaysian Block to the southeast with the Yangtze Craton to the northwest along the Jiangnan Orogenic Belt during the Neoproterozoic (e.g. Wang *et al.* 2019 and references therein). Since the Mesozoic, the South China Block has been bound by three convergent orogenic belts, with the westward subduction zone of the Pacific Plate to the east, the northward subduction and collisional belts of the Tethys to the south, and the collision belt of the North China and South China blocks along the Qinling-Dabie Orogenic Belt to the north (Li *et al.* 2012).

Southeast China includes the Cathaysian Block and the Jiangnan Orogenic Belt (Li *et al.* 2013). The Cathaysian Block has been corroborated to possess a Paleoproterozoic or even Archean basement intruded by multiple-stage igneous intrusions, especially by Mesozoic granitoids (Sun 2006 and references therein). The Cathaysian Block can be divided by the NE-trending Zhenghe-Dapu Fault

into two parts, West Cathaysia and East Cathaysia (Fig. 1), which show different geological features (Cawood *et al.* 2018; Lin *et al.* 2018). West Cathaysia mainly possesses a Neoproterozoic basement that was influenced by metamorphic and magmatic events in the Early Palaeozoic (460–420 Ma), whereas East Cathaysia comprises predominantly a Palaeoproterozoic basement overprinted by high-grade metamorphism chiefly during the Mesozoic (250–230 Ma; Lin *et al.* 2018).

The Jiangnan Orogenic Belt has a reversed S-shape, and its suture zone stretches southwestward from the Hangzhou Gulf in the northeast via Jiangshan in southwestern Zhejiang Province, Pingxiang in western Jianxi Province, Hengyang in southern Hunan Province, Yulin in the southeastern Guangxi Zhuang Autonomous Region, and Qinzhou Gulf in the southwest. This orogenic belt, which is considered part of the Grenville orogenic belt that rounded the Yangtze Craton (Li *et al.* 2010; Cawood *et al.* 2018; Wang *et al.* 2019), is dominated by early Neoproterozoic (*ca.* 1000–800 Ma) metavolcano-metasedimentary rocks that experienced greenschist-facies metamorphism (Zhou *et al.* 2002; Yao *et al.* 2014). These metamorphic sequences were intruded by Late Neoproterozoic, Early Palaeozoic and Mesozoic granitoids (Sun 2006; Wang *et al.* 2019).

The regional structures of the Southeast China region are characterized by a series of NE–NNE-trending faults. These faults (Fig. 1) either constitute the terrane boundaries (e.g. the Jiangshan-Shaoxing Fault and the Zhenghe-Dapu Fault) or form the Mesozoic–Cenozoic basin boundaries (e.g. the Suichuan-Fuzhou Fault). These NE- to NNE-trending faults dissect the region, generating a series of uplift and subsidence zones with the same strike as the faults, which have controlled the sedimentation, magmatism and mineralization in Southeast China since the Mesozoic (Thanh *et al.* 2014; Shao *et al.* 2017; Wang *et al.* 2018).

The mineral deposits in Southeast China can be classified, according to their spatial distribution, into four major metallogenic belts, from north to south, including the Mid-lower Yangtze River, Qin-Hang, Wuyishan, and Nanling metallogenic belts (Fig. 1). The Mid-lower Yangtze River and the Nanling metallogenic belts, which are located in the north and south of the Southeast China region, respectively, are not considered in this paper. The Qin-Hang Metallogenic Belt generally corresponds to the southeastern part of the Jiangnan Orogenic Belt and is 2000 km long and ~100–150 km wide. The mineralization in this belt is characterized mainly by porphyry-skarn type Cu–Pb–Zn–Ag deposits (Mao *et al.* 2011). The Wuyishan Metallogenic Belt, located in the central-eastern Cathaysia Block, contains mineralization dominated by Sn–W–REE–U deposits (Mao *et al.* 2010; Ding *et al.* 2016).

3 AMBIENT NOISE TOMOGRAPHY

3.1 Noise cross-correlation functions

In this paper, we used approximately one month of ambient noise seismic data from the Wanzai-Yongchun seismic profile (Fig. 1), with 437 EPS short-period, three-component seismographs deployed at intervals of approximately 1 km to conduct artificial (Lin *et al.* 2020; Lin *et al.* 2021) and passive-source observations (Huang *et al.* 2022) at the same time. Here, only the vertical component was used for obtaining noise cross-correlation functions.

We adopted the ambient noise data processing scheme described by Bensen *et al.* (2007) to obtain interstation noise cross-correlation functions (NCFs). The continuous ambient noise records were first

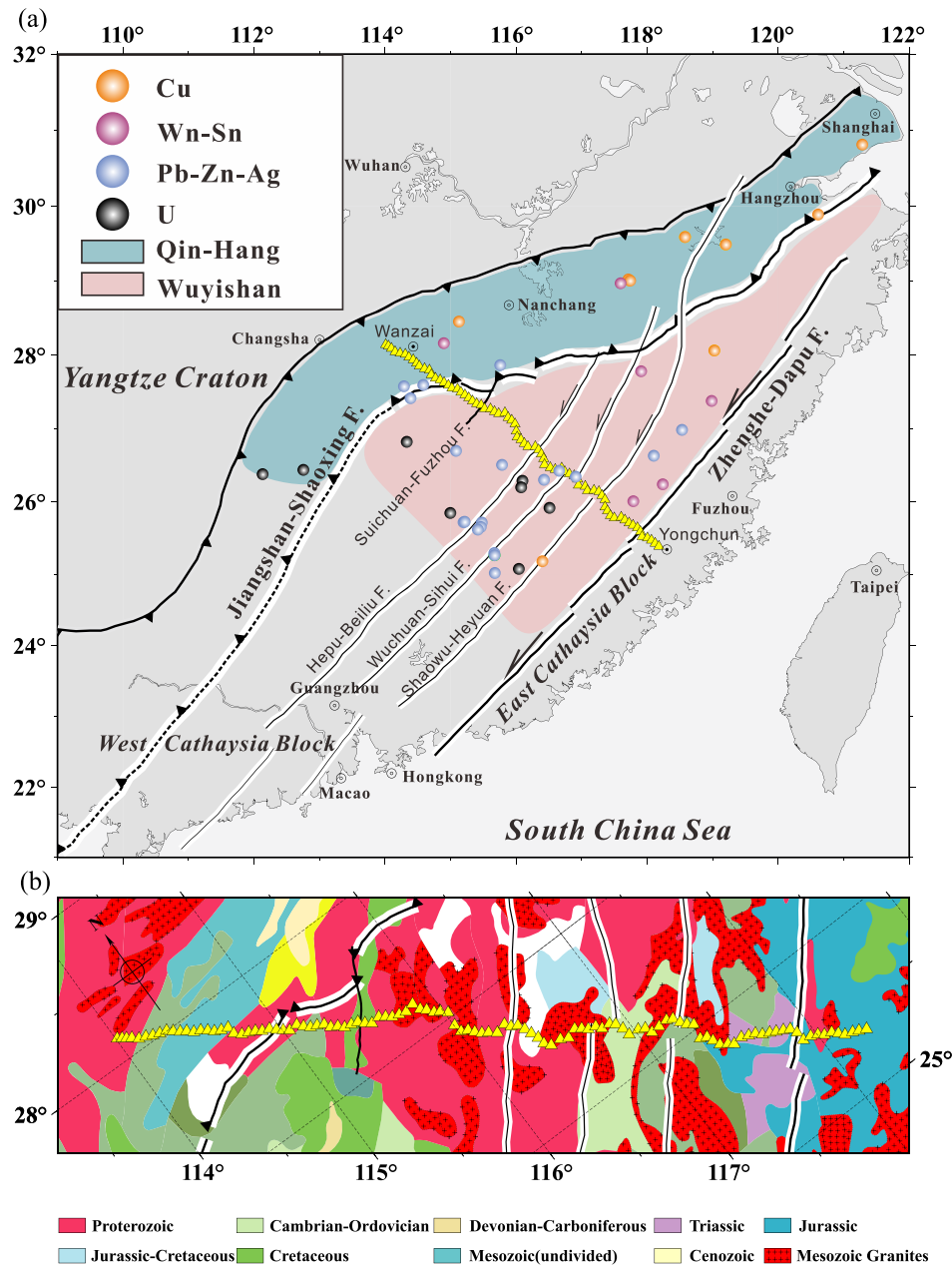


Figure 1. Area of study, tectonic and geological features, metallogenic zones and the Wanzai-Yongchun seismic profile. (a) Geological map of southeastern China with a major fracture system (Li *et al.* 2017) including the Qin-Hang and Wuyishan metallogenic belts. The yellow triangles denote the seismic stations along the Wanzai-Yongchun profile, the stations with a specific spacing are shown for esthetic reasons, as are the yellow triangles in (b). (b) Simplified geological map with strata info (Ye *et al.* 2017) around the seismic survey profile. The black lines represent regional faults, as in (a).

cut into a series of hourly segments and resampled at 20 Hz. Then, we removed the instrument response and the mean and linear trends from the raw hourly seismograms. The hourly data were then filtered at a period band of 0.3–10 s, and spectral whitening and temporal normalization were performed (using the running-absolute-mean method). Afterward, we calculated cross-correlations between all possible station pairs to obtain hourly NCFs using the pre-processed seismograms. Finally, we used the phase-weighted stacking technique (Li *et al.* 2018) to obtain the NCFs for individual station pairs.

As an example, we present the NCFs between Station 1201 and other stations in Fig. 2(a), which illustrates a strong asymmetry in its positive and negative branches. In addition, the negative branch of the normalized NCF of station pair 1201–1363 and its time-frequency analysis image are shown in Figs 2(b) and (c), respectively. Fig. 2(c) illustrates that the seismic ambient noise of the seismic records used is dominated by the energy from the period of 2.0 to 5.0 s. For all northwest–southeast source–receiver station pairs, the Rayleigh wave signal occurs only on the negative time lags. This indicates that almost all of the noise energy is from the

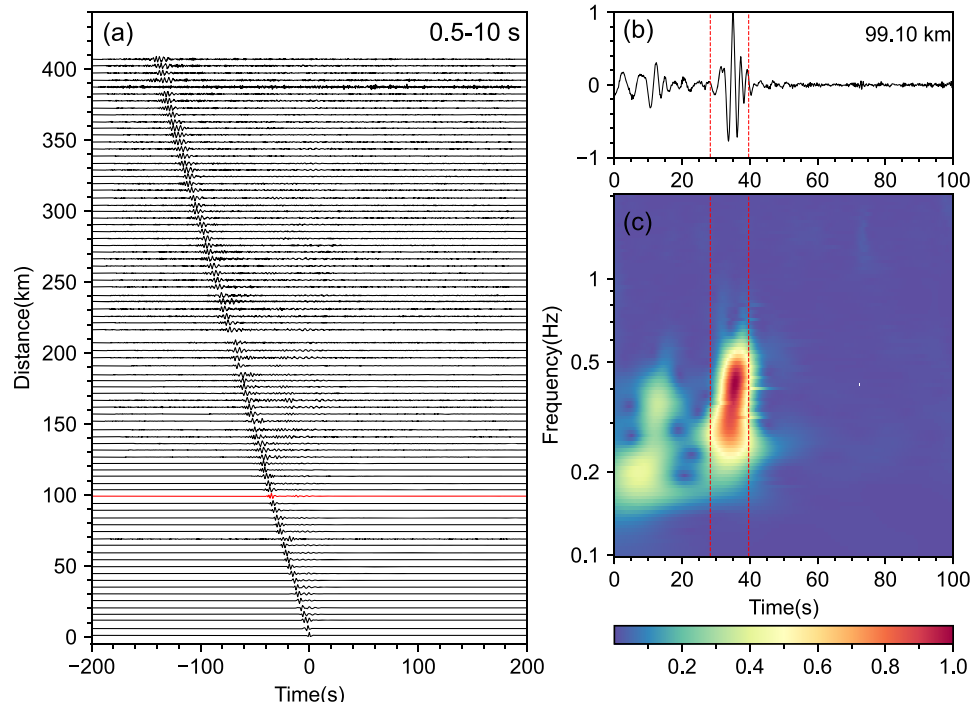


Figure 2. (a) Noise cross-correlations of the vertical component signal recorded at Station 1201 with signals recorded at other stations against interstation distances. (b) The negative branch of cross-correlations of station pair 1201–1363 separated by a distance of 99.10 km (red line in panels a) after symmetrical flipping and normalizing. (c) Time–frequency analysis of the above cross-correlation shown in panel (b) using continuous wavelet transform (Kristekova' *et al.* 2006).

Pacific Ocean caused by ocean–earth interactions (Hasselmann 1963; Nakata *et al.* 2019) and/or counterpropagating ocean wave interactions (Longuet-Higgins 1950) near the southeastern China coast. In this study, we used only the negative branches of the NCFs of all northwest–southeast source–receiver station pairs and discarded NCFs with an SNR (the ratio of the peak amplitude of the Rayleigh wave signals to the root-mean-square of the noise window) less than 15.

3.2 Rayleigh wave dispersion

We measured the Rayleigh wave phase-velocity dispersion curves using the method of Yao *et al.* (2006). We selected the station pairs with an interstation distance greater than two wavelengths to satisfy the far-field approximation. Although there is no theoretical limit to the greatest interstation distance, ignoring this issue will introduce some practical issues in the dispersion measurements and inversion. In the context of a linear, short-period, dense array, as the inner distance increases, the 2π ambiguity of phase-velocity dispersion measurements within a limited period band becomes more difficult to handle and thus introduces more measuring uncertainties, especially when automatic processing is the preferred choice for dealing with data at this scale (there are theoretically 95 266 raw paths for the 437 stations). Empirically, the long-path dispersion measurements have a limited contribution to the resolution of the final model. Therefore, we measured dispersion curves only for interstation distances shorter than 120 km (approximately eight times the wavelength of the longest period of 5 s).

After the automatic measurements, we performed a cluster analysis as described by Zheng *et al.* (2021) for quality control. In contrast to the previous study, we employed Tukey's test as a specific

criterion to identify and reject deficient or poor measurements; that is, for a given period, a measurement of less than $Q_1 - 1.5IQR$ or larger than $Q_3 + 1.5IQR$ is considered an anomaly, where Q_1 , Q_3 and IQR denote the first quartile, the third quartile and the interquartile range, respectively. Compared to the previously used three-sigma rule, this does not require the data to obey a normal distribution and is less affected by extreme anomalies, making it more appropriate for actual measurements and resulting in improved performance. Finally, we collected over 20 000 phase-velocity dispersion curves in the range of periods from 1–5 s (Figs 3a and b).

3.3 Inversion for shear wave velocity

We used the direct inversion method (Fang *et al.* 2015) to resolve the *S*-wave velocity structure beneath the Wanzai-Yongchun profile. Following the methods of Shearer (2019), we first generated the initial 1-D shear wave velocity model from the dispersion measuring data based on the empirical relationship between period/phase velocity and depth/shear wave velocity. The maximum depth for inversion was set at 14 km with an *S*-wave velocity of 3.60 km/s, while the *S*-wave velocity on the surface (0 km) was set as 2.80 km s⁻¹. Then, we discretized the 1-D velocity–depth model by interpolation, adopting varied grid sizes at different depths (Fig. 3c), and 0.5, 1.0, and 2.0 km were used for the 0–5, 5–8, and 8–14 km depth ranges, respectively.

The direct inversion algorithm we used regularly initializes model spacing along a latitude/longitude and produces a large number of grids without data perturbations for an NW–SE pseudo-linear geometry such as the one in this study (Fig. 4b), which may harm the velocity structure beneath the surveyed profile to resolve. Inspired from Wang *et al.* (2015), we used irregular grid settings at

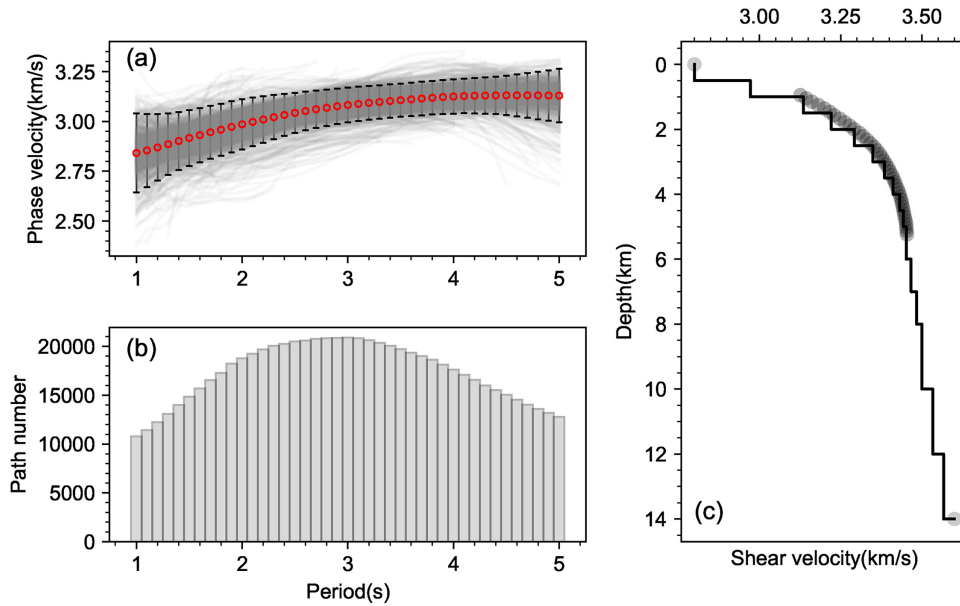


Figure 3. (a) Phase velocity dispersion curves in the period range of 1–5 s. The grey solid lines are 3000 randomly selected dispersion curves. The red circles depict the average dispersion curve, and the vertical segments are 2σ -sigma error bars for each period. (b) Bar histogram of the number of measurements for each period. (c) 1-D initial depth–velocity model. The grey circles indicate prior information deduced from the available dispersions to construct the 1-D initial model (see the main text for more details).

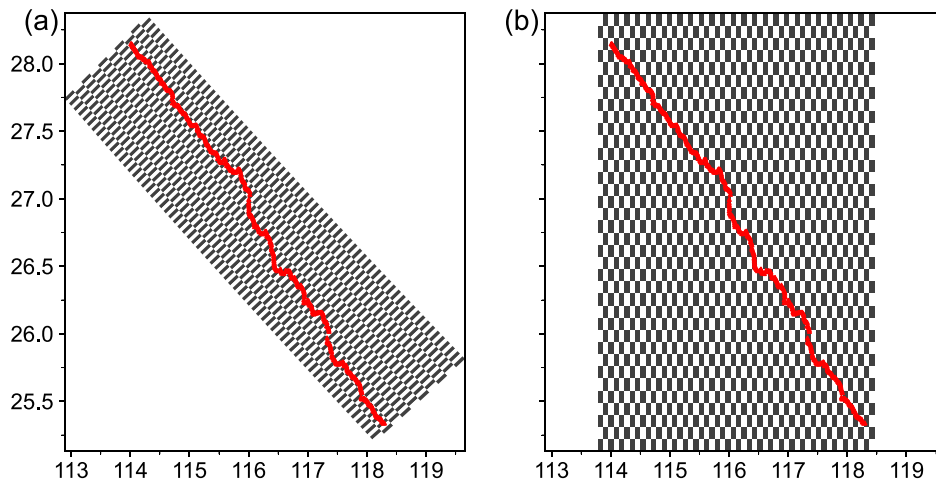


Figure 4. Model space with different grid setting. (a) Irregular grid setting using 5 km and 10 km grid spacing parallel and perpendicular to the survey line, respectively. (b) Regular grid setting using 10 and 10 km grid spacing along the longitude and latitude. In all plots, the red line shows the geometry of the seismic array.

the beginning, that is, performed the inversion under the transforming coordinates, which established a rectangular coordinate system plane in a parallel direction to the survey line (Fig. 4a). Under the transforming coordinates, we adopted a grid size of 5×10 km (in a direction parallel and perpendicular to the survey line) to perform the inversion and determined the velocity structure beneath the profile. However, this strategy introduces a slight (usually acceptable) systematic bias to the inversion because the interstation distance calculated under the original and transforming coordinates are slightly different for the same station pair (Wang *et al.* 2015). Meanwhile, we also performed direct inversion using regular grid settings (Fig. 4b). When a grid size of 10×10 km was used, the

model (Fig. 5b) was comparable to the S -wave model using a grid size of 5×10 km under the transforming coordinates (Fig. 5a) with similar first-order velocity features.

Since this approach (Fang *et al.* 2015) was originally used to resolve 3-D variations of the shear wave, analysing or testing the lateral resolution of the model under the field data distribution and inverse settings is required for this nearly linear, NW–SE geometry. Therefore, we carried out a checkerboard test for inversion using irregular grid settings (Fig. 6) and regular settings (Fig. 7). For both settings, we designed a checkerboard input model considering only a lateral resolution, that is, consisting of alternate velocity anomalies of approximately ± 10 per cent that were oriented

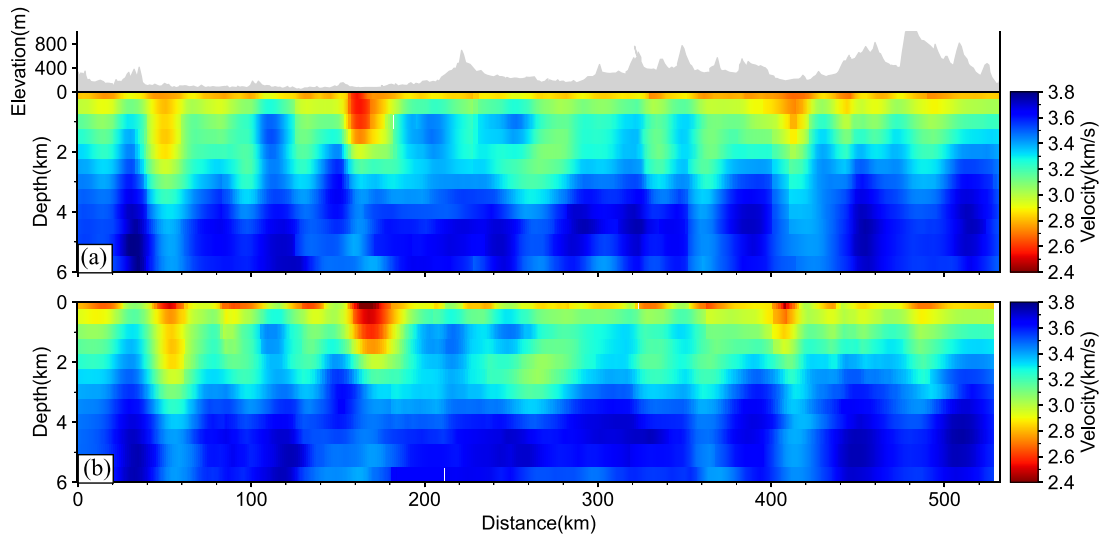


Figure 5. 2-D distance–depth *S*-wave velocity cross-sections solved using first (a) an irregular grid setting (Fig. 4a), and then (b) a regular grid setting (Fig. 4b).

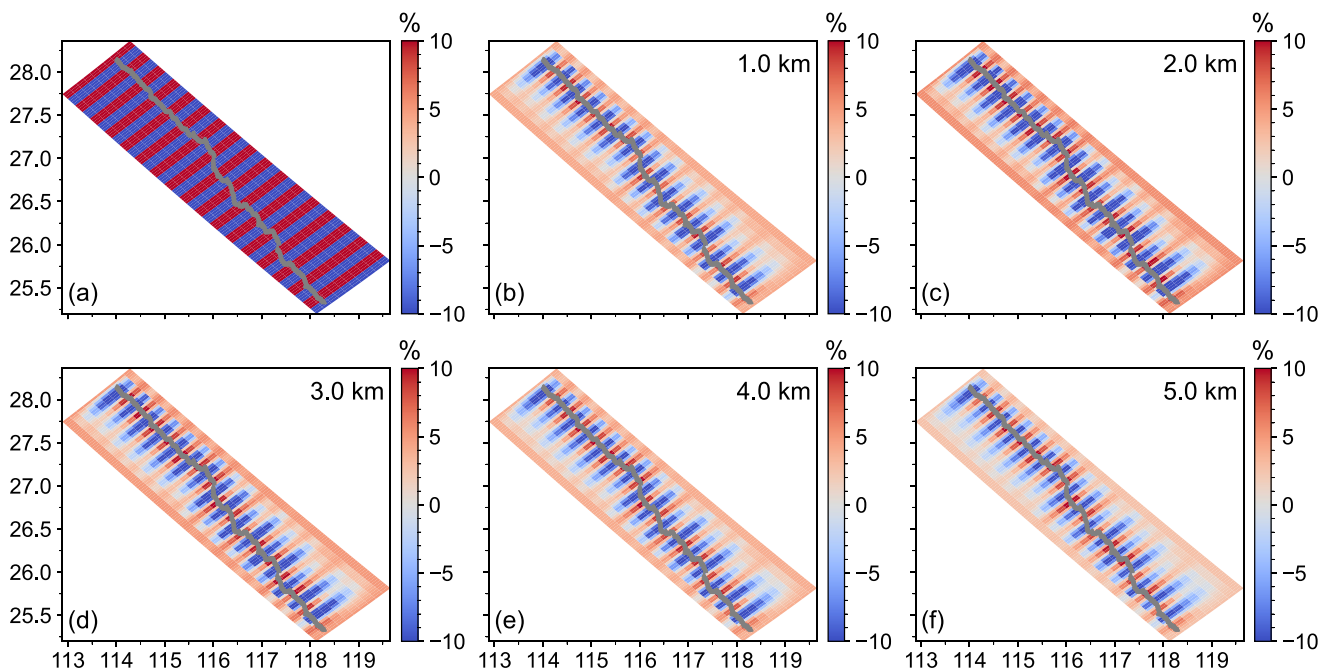


Figure 6. Checkerboard test for inversion using an irregular grid setting. (a) Input model (in percentage of change in *S*-wave velocity). (b)–(f) Horizontal depth slices of the recovered model at depths of 1–5 km (see colour scale on the right). In all plots, the grey line shows the geometry of the survey array.

perpendicular to the nearly linear geometry of the profile (Figs 6a and 7a). Several horizontal depth slices of the recovered model at various depths (Figs 6b–f and 7b–f) revealed a recognizable velocity pattern near the survey array where sufficient data constraints were provided, confirming that the lateral variations of the model can be well determined and providing a reliable and interpretable anomaly size. The lateral resolution can reach 20 and 30 km for irregular and regular grid settings, respectively. It should be noted that every depth slice (Figs 7b–f) was clipped to highlight the velocity variations along the survey array when using the regular grid settings.

For a certain period, the fundamental-mode Rayleigh wave was mostly sensitive to the *S*-wave velocity at approximately one-third

of the wavelength. To evaluate the robustness and resolution of the *S*-wave velocity against depth, we computed the phase-velocity sensitivity kernels with respect to the *S*-wave velocity. The *S*-wave velocity 1-D depth model, shown in Fig. 8(a), was the same as Fig. 3(c), which was utilized to calculate the phase-velocity sensitivity kernel curves. The *P*-wave velocity model was constructed based on the empirical relationship with the *S*-wave velocity ($V_p/V_s = 1.73$), and the density value was set to a constant (2.60 kg/m^3). Fig. 8(b) shows the peak values of the sensitivity kernels at different sample periods for the given reference model. Fig. 8(c) shows the Rayleigh wave phase-velocity sensitivity against depth within the period ranging from 1.0 to 5.0 s. The most sensitive depth of the maximum period of 5.0 s was approximately

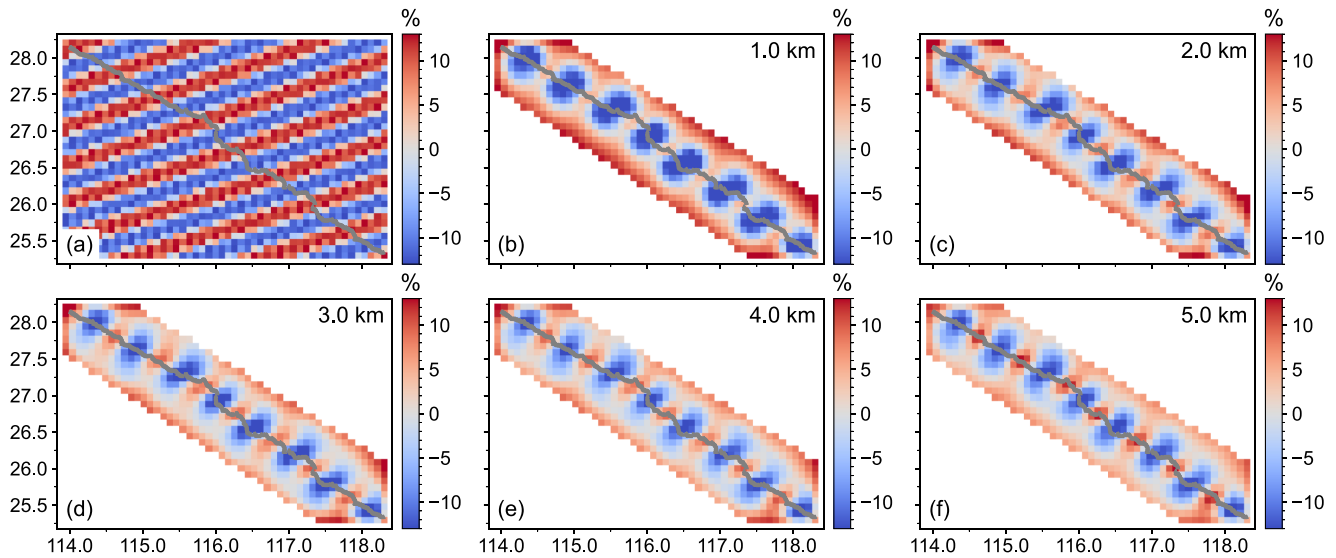


Figure 7. Checkerboard test for inversion using a regular grid setting. (a) Input model (in percentage of change in S -wave velocity). (b–f) Horizontal depth slices of the recovered model at depths of 1–5 km (see colour scale on the right). To highlight the velocity variations along the survey array, every depth slice was clipped. In all plots, the grey line shows the geometry of the survey array.

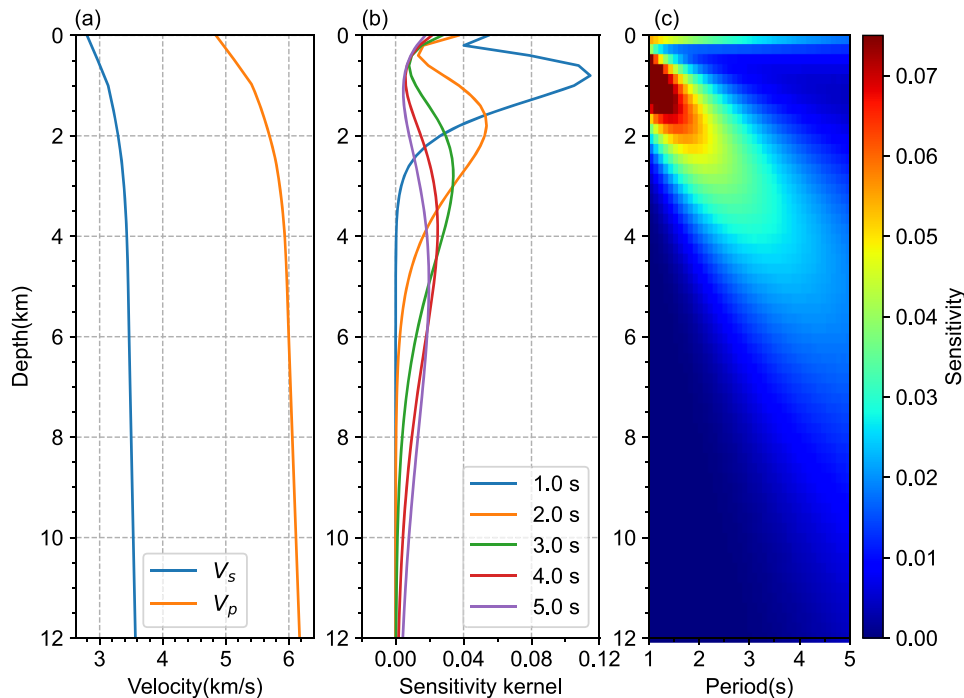


Figure 8. Rayleigh wave phase-velocity sensitivity kernel analysis. (a) 1-D local average velocity–depth model, as in Fig. 3(c). (b) Rayleigh wave phase-velocity sensitivity kernels with respect to S -wave velocity for periods of 1.0, 2.0, 3.0, 4.0 and 5.0 s. (c) Rayleigh wave phase-velocity sensitivity against depth for periods ranging from 1.0 to 5.0 s.

6 km, while the depth available for interpretation can be empirically greater. However, to compare the S -wave and P -wave velocity models in the overlapping depth (0–6 km) and spatial ranges (red triangles in Fig. 1), we focused only on the S -wave velocity structure above the 6 km depth. The S -wave velocity at each depth beneath every seismic station was determined by using 2-D cubic spline interpolation, and then a 2-D distance–depth S -wave velocity cross-section was constructed (Fig. 5), which was gridded using adjustable tension continuous curvature spline interpolation (Fig. 9b).

4 DISCUSSION

4.1 V_p/V_s model construction and correlation with geological observations

These active- and passive-source observations allow us to compare different velocity models obtained from different seismic data sets and related methods. Overall, the fact that consistent structural patterns were exhibited in the S -wave (Fig. 9b) and P -wave (Fig. 9c)

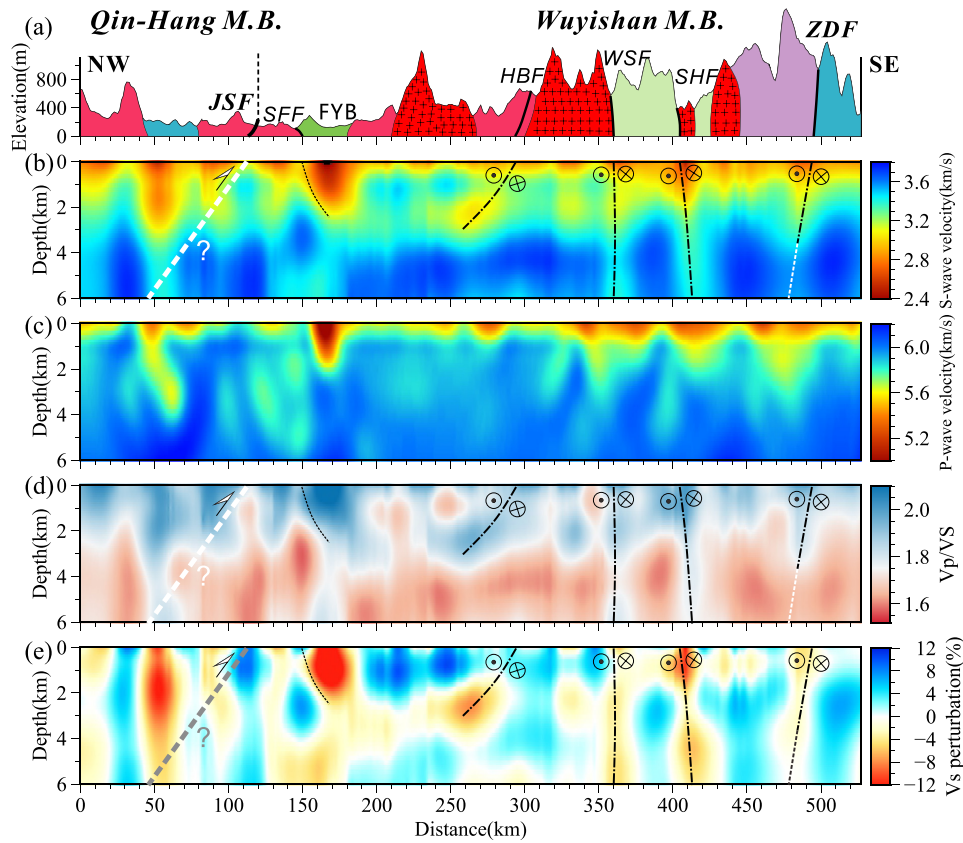


Figure 9. (a) Elevation and strata info across the survey line, including the Qin-Hang (Qin-Hang M.B.) and Wuyishan (Qin-Hang M.B.) metallogenic belts and regional faults. The strata colour map settings are the same as those in Fig. 1(b). Acronyms: JSF, Jiangshan-Shaoxing Fault; SFF, Suichuan-Fuzhou Fault; FYB, Fuzhou-Yongfeng Basin; HBF, Hepu-Beiliu Fault; WSF, Wuchuan-Sihui Fault; SHF, Shaowu-Heyuan Fault; ZDF, Zhenghe-Dapu Fault. (b) S -wave velocity model obtained from seismic ambient noise tomography. (c) P -wave velocity model revealed by first-arrival travel-time tomography (Lin *et al.* 2020). (d) The ratio of seismic P -wave and S -wave velocities calculated from the previous S - and P -velocity models. (e) The S -wave velocity perturbation model derived from (b).

velocity models, which were determined by ambient noise surface wave tomography and first-arrival travel-time tomography (Lin *et al.* 2020), respectively, implied that both velocity models were generally reliable. For example, in these two models, we observed a shallow low-velocity zone on the SE side of the Suichuan-Fuzhou Fault, as well as a similar seismic velocity structural pattern below the Wuchuan-Sihui Fault and Zhenghe-Dapu Fault.

Nevertheless, using the obtained S -wave and P -wave velocity models, we derived the V_p/V_s ratio model (Fig. 9d) by dividing the V_p by V_s models. To mitigate for potentially extreme inaccuracies and numerical artefacts due to simply dividing the V_p by V_s models obtained from data with differing resolutions (Berg *et al.* 2021), we resampled the V_p model based on the V_s model's grid setting before dividing the V_p by V_s models. In addition, we calculated the S -wave velocity perturbation model (Fig. 9e) to capture seismic velocity anomalies better.

These seismic velocity models (Fig. 9) revealed a strong lateral velocity variation in the shallow upper crust below the Wanzai-Yongchun profile. At the shallow crust scale, seismic velocities (anomalies) can be affected by rock composition and porosity, the presence of fluids, fracture/fault structure, etc. In our seismic velocity models, we observed a good correlation between the seismic velocity anomalies and the spatial distribution of faults (zones) and sedimentary basins.

On both sides of the Jiangshan-Shaoxing Fault, we found two seismic velocity anomalies (low S -wave and P -wave velocities and a low S -wave perturbation) at depths of 0~2 km (Figs 9b–e). The anomaly on the SE side is located where the known Mesozoic Fuzhou–Yongfeng Basin occurs at the surface (Fig. 9a). This basin was formed by fault tilting and is filled by molasse-like continental sediment, including purple–red glutenite, sandstone, and siltstone, with basaltic interbeds inside (Zhang *et al.* 2015). The high V_p/V_s (Fig. 9d) and reduced V_s values (Fig. 9b) are also in line with typical seismic features of sedimentary basins. The neighbored Suichuan-Fuzhou Fault, which formed during the Mesozoic, has controlled the formation of the lithology, basin, and ore deposits in the adjacent area (Zhang *et al.* 2015), and the fault lies on a high- and low-resistivity gradient line, as revealed by a magnetotelluric (MT) geophysical survey. Therefore, we deduced the deep extension and shape of this fault based on the shape of its controlling sedimentary basin and surface geological observations (Fig. 9).

The other anomaly is on the NW side of the Jiangshan-Shaoxing Fault, that is, within the range of the Qin-Hang Metallogenic Belt (i.e. the Jiangnan orogenic belt). Geological studies have shown that in addition to Mesozoic strata, Proterozoic low-grade metamorphic volcanic-sedimentary rock series also occur in the area, for example the continental margin clastic deposition of the Shuangqiaoshan Group, Fanjingshan Group, Sibao Group, Lengjiayi Group and

Shangxi Group (879–823 Ma, Ni & Wang 2017). We thus suggest that this low seismic velocity anomaly could be partially ascribed to the Proterozoic volcanic–sedimentary rock series, as well as the overlying sedimentary strata.

Regarding the Jiangshan-Shaoxing Fault, it is a lithospheric-scale fault (zone) that used to be considered the suture between the Yangtze and Cathaysian blocks, although its tectonic attributes are controversial (He *et al.* 2013; Guo & Gao 2018; Guo *et al.* 2019). Fig. 9 gives a possible extension shape of this fault (marked by the light dashed line) deduced from the geological data (Li *et al.* 2017). However, our models seem to fail to capture the indications of this fault zone. One possible reason for this failure is that the fault zone has been re-constructed with more complicated architecture and composition by subsequent tectonic activities since it formed. Additionally, the non-orthogonality between the seismic array and the fault's strike could contribute to the failure to capture the fault.

Within the core region of the Wuyishan Metallogenic Belt, generally corresponding to the area of Wuyi Mountain, several narrow, elongated and low seismic velocity anomalies show a good correlation with the spatial location of regional faults (e.g. the Hepu-Beiliu, Wuchuan-Sihui, Shaowu-Heyuan and Zhenghe-Dapu faults). These seismic velocity anomalies exhibit the attributes of low *S*-wave (perturbation) anomalies and relatively high *V_p/V_s* ratios, which are typical features of the fault zone because faulting usually generates fragmentation and cataclysm, and even the circulation of fluids. In addition, the average lateral width of these seismic velocity anomalies is approximately 20 km (Figs 9b and e), which is equal or slightly higher than the fault size estimate based on the geological survey (Liu 1997; Shui & Shi 1997; Wang *et al.* 2009). Therefore, we interpret these seismic velocity anomalies as indications of the regional fault zones. Basically, we deduce the possible extensions and patterns of these regional faults at depth based on the shapes of these seismic velocity anomalies, the reasonability of which can be validated by the consistency with the surface geological evidence. For example, the Wuchuan-Sihui and Shaowu-Heyuan faults may run through the upper crust with large dip angles based on the obtained seismic models (Fig. 9), which is consistent with the strike-slip properties obtained from surface geological observations (Liu *et al.* 2009; Li *et al.* 2017).

4.2 Fault system in Wuyishan and its effect on regional metallogeny

The Suichuan-Fuzhou Fault, located on the NW margin of the Wuyishan Metallogenic Belt, is a typical tensional and/or transtensional fault in this region and is considered to control the development of the Fuzhou–Yongfeng Basin (Zhang *et al.* 2015). A series of studies suggest that the tensional and/or transtensional faults in this region play a role in promoting the occurrence and development of volcanic–sedimentary basins and U and Pb–Zn–Ag deposits. For example, Xiangshan, a typical large-scale U deposit associated with ultrashallow emplaced subvolcanic rocks, is located on a large faulted volcanic basin (Zhang *et al.* 2015) and occurs in a composite site of NE-trending structures and annular volcanic collapse structures inside the subvolcanic body and its outer contact zone (Chen *et al.* 2012); Lengshuikeng, a large-scale Pb–Zn–Ag deposit related to an alkaline granite porphyry (*ca.* 163 Ma, Meng *et al.* 2009), occurs along the edge of the Yuefengshan Mesozoic volcanic basin. The ore-bearing porphyry is alkaline granite intruding into the Jurassic volcanic rocks during the Middle Yanshanian Period, and a large

number of crypto explosion breccia developed around the edge of the ore-bearing porphyry (Meng *et al.* 2009).

Within the core region of the Wuyishan Metallogenic Belt, a series of large representative strike-slip faults, including the Hepu-Beiliu, Wuchuan-Sihui and Shaowu-Heyuan faults, developed in the Jurassic and were strongly reactivated during the Early Cretaceous (Xu *et al.* 1985), and these faults mainly manifested as dextral strike-slip mode. These faults are considered to have formed during the low-angle subduction of the Palaeo-Pacific Plate since the Cretaceous and governed the emergence and development of hundreds of pull-apart volcano-sedimentary basins (Li *et al.* 2017). A large number of ore deposits occurred along these fault and basin zones that are considered to control the uranium–gold–zinc mineralization of the Wuyishan metallogenic belt (Yang & Yao 2008). Considering the association between metallogenic activities and magmatic eruptions in this area and the general depth extension of these faults mapped by the obtained models (Fig. 9), we suggest that these faults, as the ore-guiding structures, promote the migration and diffusion of ore-forming fluids during magmatic and metallogenic activities. Additionally, based on surface geology evidence, Ding *et al.* (2016) suggested that the Wuyishan Metallogenic Belt can be dissected into several subunits by several strike-dip faults and this partition nature is also confirmed by the obtained seismic velocity structure (Fig. 9).

Previous studies (Xu *et al.* 2014; Lin *et al.* 2021; Liu *et al.* 2021; Zhang *et al.* 2021a,c; Hou *et al.* 2022) suggest that the crustal compositional structure (especially in lower crust) is likely the fundamental factor affecting the regional metallogenic differences. However, considering the close association between the deposit types and the regional faults in Wuyishan and the impacted scope and pattern of the fault zones constrained by the obtained models (Fig. 9), we suggest that fault systems and their effect on the shallow crust could also contribute to the regional metallogenic differences.

5 CONCLUSIONS

The obtained seismic velocity models show a good correlation with geological observations. The Fuzhou–Yongfeng Basin and Proterozoic volcanic–sedimentary rock series are characterized by low *P*- and *S*-wave velocities, high *V_p/V_s* ratios and low *S*-wave velocity perturbations. Within the core region of the Wuyishan Metallogenic Belt, a series of narrow, elongated and low seismic velocity anomalies are interpreted as indications of the regional fault zones and provide reference information on the extension and pattern of these faults at depth. In combination with the geological and mineralogical evidence, we suggest that these faults play a role as the ore-guiding structures and promote the formation of regionally representative mineral species and metal assemblages.

ACKNOWLEDGMENTS

We thank two reviewers François Lavoué and Stephen Gao, assistant editor Louise Alexander and editor Andrea Morelli for constructive comments and suggestions that helped us to improve the manuscript. We would like to thank the Geophysical Exploration Center, China Earthquake Administration for its contribution to seismic data acquisition. We are very grateful to Profs. Laicheng Miao, Huajian Yao, Yingjie Yang, Yonghua Li and Yong Zheng for the helpful advices. The National Natural Science Foundation of China (42130807 and 41974048) and the National Key Research

and Development Program of China (2016YFC0600201) funded this study.

DATA AVAILABILITY

The data that support the findings of this study are available from the Institute of Geology and Geophysics, Chinese Academy of Sciences (IGGCAS) but restrictions apply to the availability of these data, which were used under license for this study, and so are not publicly available for now. We declare that this paper has not been submitted elsewhere.

CONFLICT OF INTEREST

The authors declare that they have no known competing financial interests or personal relationships that could have appeared to influence the work reported in this paper.

REFERENCES

- Bensen, G.D., Ritzwoller, M.H., Barmin, M.P., Levshin, A.L., Lin, F.C., Moschetti, M.P., Shapiro, N.M. & Yang, Y., 2007. Processing seismic ambient noise data to obtain reliable broad-band surface wave dispersion measurements, *Geophys. J. Int.*, **169**, 1239–1260.
- Berg, E.M., Lin, F.C., Schulte-Pelkum, V., Allam, A., Qiu, H. & Gkogkas, K., 2021. Shallow crustal shear velocity and Vp/Vs across Southern California: joint inversion of short-period Rayleigh wave ellipticity, phase velocity, and teleseismic receiver functions, *Geophys. Res. Lett.*, **48**, e2021GL092626.
- Cawood, P.A., Zhao, G., Yao, J., Wang, W., Xu, Y. & Wang, Y., 2018. Reconstructing South China in Phanerozoic and Precambrian supercontinents, *Earth Sci. Rev.*, **186**, 173–194.
- Chen, Z., Han, F., Yang, N., Wang, P., Gong, H., Shao, F., Tang, X., Xu, J., Zhou, Y. & Wang, Y., 2012. Topographic erosive diversities of the Xiangshan uranium ore-field, Jiangxi province and its implications for ore-preservation: evidences from fission track dating of apatite, *Chinese J. Geophys.*, **55**, 2371–2384 (in Chinese).
- Ding, J., Fan, J., Yin, J. & Liu, Y., 2016. Geological Characteristics and mineral resource potential of the Wuyishan CuPb zn polymetallic metallogenic belt, *Acta Geol. Sin.*, **90**, 1537–1550.
- Fang, H., Yao, H., Zhang, H., Huang, Y.-C. & van der Hilst, R.D., 2015. Direct inversion of surface wave dispersion for three-dimensional shallow crustal structure based on ray tracing: methodology and application, *Geophys. J. Int.*, **201**, 1251–1263.
- Guo, L. & Gao, R., 2018. Potential-field evidence for the tectonic boundaries of the central and western Jiangnan belt in South China, *Precambrian Res.*, **309**, 45–55.
- Guo, L., Gao, R., Shi, L., Huang, Z. & Ma, Y., 2019. Crustal thickness and Poisson's ratios of South China revealed from joint inversion of receiver function and gravity data, *Earth planet. Sci. Lett.*, **510**, 142–152.
- Hasselmann, K., 1963. A statistical analysis of the generation of microseisms, *Rev. Geophys.*, **1**, 177–210.
- He, C., Dong, S., Santosh, M. & Chen, X., 2013. Seismic evidence for a geosuture between the Yangtze and Cathaysia Blocks, South China, *Sci. Rep.*, **3**, 2200.
- He, C. & Santosh, M., 2016. Crustal evolution and metallogeny in relation to mantle dynamics: a perspective from P-wave tomography of the South China Block, *Lithos*, **263**, 3–14.
- Hou, J., Xu, T., Lü, Q., Bai, Z., Zhang, Y., Zhang, Z. & Deng, Y., 2022. The deep background of large-scale, Mesozoic Cu–Au–W metallogenesis in northeastern South China: constraints from Yingshan–Changshan wide-angle seismic reflection/refraction data. *Sci. China Earth Sci.*, doi:10.1007/s11430-022-9973-4.
- Huang, M., Xu, T., Lü, Q., Lin, J., Bai, Z., Deng, Y., Zhang, Y. & Badal, J., 2022. Crustal structure along the Wanzai–Yongchun profile in the Cathaysia Block, Southeast China, constrained by a joint active- and passive-source seismic experiment, *Geophys. J. Int.*, **231**, 384–393.
- Kristekova', M., Kristek, J., Moczo, P. & Day, S.M., 2006. Misfit criteria for quantitative comparison of seismograms, *Bull. seism. Soc. Am.*, **96**, 1836–1850.
- Li, G., Niu, F., Yang, Y. & Xie, J., 2018. An investigation of time–frequency domain phase-weighted stacking and its application to phase-velocity extraction from ambient noise's empirical Green's functions, *Geophys. J. Int.*, **212**, 1143–1156.
- Li, S., Santosh, M., Zhao, G., Zhang, G. & Jin, C., 2012. Intracontinental deformation in a frontier of super-convergence: a perspective on the tectonic milieu of the South China Block, *J. Asian Earth Sci.*, **49**, 313–329.
- Li, S., Zang, Y., Wang, P., Suo, Y., Li, X., Liu, X., Zhou, Z., Liu, X. & Wang, Q., 2017. Mesozoic tectonic transition in South China and initiation of Palaeo-Pacific subduction, *Earth Sci. Front.*, **24**, 213–225 (in Chinese).
- Li, X., Hu, R., Hua, R., Ma, D., Wu, L., Qi, Y. & Peng, J., 2013. The Mesozoic syntaxis type granite-related Cu–Pb–Zn mineralization in South China, *Acta Geol. Sin.*, **29**, 4037–4050 (in Chinese).
- Li, X., Wang, C., Hua, R. & Wei, X., 2010. Fluid origin and structural enhancement during mineralization of the Jinshan orogenic gold deposit, South China, *Miner. Deposita*, **45**, 583–597.
- Lin, J., Tang, G., Xu, T., Cai, H., Lü, Q., Bai, Z., Deng, Y., Huang, M. & Jin, X., 2020. P-wave velocity structure in upper crust and crystalline basement of the Qinhang and Wuyishan Metallogenic belts: constraint from the Wanzai–Hui'an deep seismic sounding profile, *Chin. J. Geophys.*, **63**, 4396–4409 (in Chinese).
- Lin, J., Xu, T., Cai, H., Lü, Q., Bai, Z., Deng, Y., Zhang, Y., Huang, M., Badal, J. & Jin, X., 2021. Crustal velocity structure of Cathaysia Block from an active-source seismic profile between Wanzai and Hui'an in SE China, *Tectonophysics*, **811**, 228874.
- Lin, S., Xing, G., Davis, D.W., Yin, C., Wu, M., Li, L., Jiang, Y. & Chen, Z., 2018. Appalachian-style multi-terrane Wilson cycle model for the assembly of South China, *Geology*, **46**, 319–322.
- Liu, C., Yin, W., Zhang, J., Zeng, L. & OuYang, K., 2009. Ore-controlling factors and prospecting prediction criteria of the Sn–Cu polymetallic deposit in Wuyishan metallogenic zone, *Miner. Resour. Geol.*, **35**, 124–128 (in Chinese).
- Liu, D., 1997. Segmentation of the Shaowu–Heyuan Fault Zone and their activity assessment, *J. Geomech.*, **3**, 54–60 (in Chinese).
- Liu, W., Lü, Q., Cheng, Z., Xing, G., Yan, J., Yuan, L. & Chen, C., 2021. Multi-element geochemical data mining: implications for block boundaries and deposit distributions in South China, *Ore Geol. Rev.*, **133**, 104063.
- Longuet-Higgins M.S., 1950. Please place the cursor inside editing element., *Philos. Trans. R. Soc. A Math. Phys. Eng. Sci.*, **243**, 1–35.
- Mao, J., Chen, M., Yuan, S. & Guo, C., 2011. Geological Characteristics of the Qinhang (or Shihang) Metallogenic Belt in South China and spatial-temporal distribution regularity of mineral deposits, *Acta Geol. Sin.*, **85**, 635–658 (in Chinese).
- Mao, J., Xie, G., Cheng, Y. & Chen, Y., 2009. Mineral deposit models of mesozoic ore deposits in South China, *Geological Rev.*, **55**, 347–354 (in Chinese).
- Mao, J., Zhao, X., Ye, H.M., Hu, Q., Liu, K. & Yang, F., 2010. Tectono-magmatic mineralization and evolution in Wuyishan metallogenic belt, *Shanghai Geol.*, **31**, 140–144 (in Chinese).
- Meng, X., Hou, Z., Dong, G., Liu, J., Zuo, L., Yang, Z. & Xiao, M., 2009. Geological Characteristics and Mineralization Timing of the Lengshuikeng Porphyry Pb–Zn–Ag Deposit, Jiangxi Province, *Acta Geologica Sinica*, **83**, 1951–1967 (in Chinese).
- Nakata, N., Gualtieri, L. & Fichtner, A., 2019. *Seismic Ambient Noise*, Cambridge Univ. Press.
- Ni, P. & Wang, G.-G., 2017. Multiple episodes of Cu–Au mineralization in the northeastern section of the Qin–Hang metallogenic belt induced by reworking of continental crust, *Acta Petrol. Sin.*, **33**, 3373–3394 (in Chinese).
- O'Donnell, J., Thiel, S., Robertson, K., Gorbato, A. & Eakin, C., 2020. Using seismic tomography to inform mineral exploration in South Australia: the AusArray SA broadband seismic array, *MESA J.*, **93**, 24–31.

- Shao, L., Cao, L., Qiao, P., Zhang, X., Li, Q. & van Hinsbergen, D.J.J., 2017. Cretaceous–Eocene provenance connections between the Palawan Continental Terrane and the northern South China Sea margin, *Earth planet. Sci. Lett.*, **477**, 97–107.
- Shearer, P.M., 2019. *Introduction to Seismology*, Cambridge Univ. Press.
- Shui, T., Shi, H. & Pan, M., 1997. Deformation analysis of tectonic rocks in Wuchuan-Sihui faulting belts, *Volcanol. Miner. Resour.*, **18**, 191–202 (in Chinese).
- Sun, T., 2006. A new map showing the distribution of granites in South China and its explanatory notes, *Geol. Bull. China*, **25**, 332–335 (in Chinese).
- Thanh, N.X., Hai, T.T., Hoang, N., Lan, V.Q., Kwon, S., Itaya, T. & Santosh, M., 2014. Backarc mafic–ultramafic magmatism in Northeastern Vietnam and its regional tectonic significance, *J. Asian Earth Sci.*, **90**, 45–60.
- Wang, M., Chen, Y., Liang, X., Xu, Y., Fan, Y., Xu, T., Zhang, Z. & Teng, J., 2015. Surface wave tomography for South China and the northern South China Sea area, *Chin. J. Geophys.*, **58**, 1963–1975 (in Chinese).
- Wang, M., Zhou, B., Ji, F., Chen, X. & Chen, G., 2009. Fault activity on the Hepu Basin Section of the Hepu-Beiliu Fault, *Seismol. Geol.*, **31**, 470–487 (in Chinese).
- Wang, R., Wang, Q., Huang, Y., Yang, S., Liu, X. & Zhou, Q., 2018. Combined tectonic and paleogeographic controls on the genesis of bauxite in the Early Carboniferous to Permian Central Yangtze Island, *Ore Geol. Rev.*, **101**, 468–480.
- Wang, Y., Zhu, W., Huang, H., Zhong, H., Bai, Z., Fan, H. & Yang, Y., 2019. Ca. 1.04 Ga hot Grenville granites in the western Yangtze Block, southwest China, *Precambrian Res.*, **328**, 217–234.
- Xing, G., Hong, W., Zhang, X., Zhao, X., Ban, Y. & Xiao, F., 2017. Yanshanian granitic magmatism and their mineralizations in East China, *Acta Geol. Sin.*, **33**, 1571–1590 (in Chinese).
- Xu, J., Cui, K., Liu, Q., Tong, W. & Zhu, G., 1985. Mesozoic sinistral transcurrent faulting along the continent margin in eastern Asia, *Mar. Geol. Quat. Geology*, **5**, 51–64. (in Chinese).
- Xu, T., Zhang, Z., Tian, X., Liu, B., Bai, Z., Lü, Q. & Teng, J., 2014. Crustal structure beneath the Middle-Lower Yangtze metallogenic belt and its surrounding areas: constraints from active source seismic experiment along the Lixian to Yixing profile in East China, *Acta Geol. Sin.*, **30**, 918–930 (in Chinese).
- Yang, M. & Yao, J., 2008. Prospecting evaluation of the W, Sn, Cu, Au, Ag metallogenic belt in Wuyishan area, *Miner. Resour. Geol.*, **22**, 33–35 (in Chinese).
- Yao, H.J., van Der Hilst, R.D. & de Hoop, M.V., 2006. Surface-wave array tomography in SE Tibet from ambient seismic noise and two-station analysis—I. Phase velocity maps, *Geophys. J. Int.*, **166**, 732–744.
- Yao, J., Shu, L. & Santosh, M., 2014. Neoproterozoic arc-trench system and breakup of the South China Craton: constraints from N-MORB type and arc-related mafic rocks, and anorogenic granite in the Jiangnan orogenic belt, *Precambrian Res.*, **247**, 187–207.
- Ye, T., Huang, C. & Deng, Z., 2017. Spatial database of 1: 2500000 digital geologic map of People’s Republic of China, *Geology in China*, **44**, 19–24 (in Chinese).
- Zhang, W., Li, Z., Liu, D. & Zhao, Y., 2015. The tectonic activity trail of Fuzhou-Yong Feng fault and its significance to uranium ore exploration in central Jiangxi province, *Contrib. Geol. Miner. Res. Res.*, **30**, 23–29 (in Chinese).
- Zhang, Y., Shi, D., Lü, Q., Xu, Y., Xu, Z., Gong, X., Yan, J. & Xu, T., 2021c. A fine crustal structure and geodynamics revealed by receiver functions along the Guangchang-Putian line in the Cathaysia Block, South China, *Tectonophysics*, **815**, 229007.
- Zhang, Y., Shi, D., Lü, Q., Xu, Y., Xu, Z., Yan, J., Chen, C. & Xu, T., 2021a. The crustal thickness and composition in the eastern South China Block constrained by receiver functions: implications for the geological setting and metallogenesis, *Ore Geol. Rev.*, **130**, 103988.
- Zhang, Z., Deng, Y., Yao, J., Zong, J. & Chen, H., 2021b. An array based seismic image on the Dahutang deposit, South China: insight into the mineralization, *Phys. Earth planet. Inter.*, **310**, 106617.
- Zheng, M., Bai, Z., Xu, T. & Badal, J., 2021. Upper crustal velocity structure of the Ailaoshan-Red River shear zone and its implication for Cenozoic tectonic-magmatic activity: evidence from ambient noise tomography using short-period dense seismic array, *Phys. Earth planet. Inter.*, **311**, 106643.
- Zhou, M.-F., Yan, D.-P., Kennedy, A.K., Li, Y. & Ding, J., 2002. SHRIMP U–Pb zircon geochronological and geochemical evidence for Neoproterozoic arc-magmatism along the western margin of the Yangtze Block, South China, *Earth planet. Sci. Lett.*, **196**, 51–67.